Arabian Journal for Science and Engineering (2024) 49:10599–10612
https://doi.org/10.1007/s13369-023-08322-6

RESEARCH ARTICLE-MECHANICAL ENGINEERING

Enhancement of the Hygrothermoelastic Performance of Rotating Cylindrical Smart Sensors

A. M. Eldeeb[1] · **Y. M. Shabana**[1,2] · **A. Elsawaf**[3]

Received: 14 February 2023 / Accepted: 17 September 2023 / Published online: 14 November 2023

Abstract

The goal of this research article is to investigate the effects of using two-dimensional functionally graded materials on the performance of piezoelectric sensors/actuators when subjected to simultaneous complex loading conditions. The considered disc-shaped sensors/actuators have nonuniform thicknesses and undergo asymmetric hygro-thermo-electro-mechanical loading. A power-law model is used to grade the materials radially, whereas the cosine function, which includes two independent parameters, describes the pattern along the circumferential direction. Comparing the results obtained by using the finite element method with those of one-dimensional graded structures leads to promising outcomes. For example, the radial displacement exhibits vital changes that varied between −13 and 31%. This is beneficial for such structures in terms of enhancing their sensing/actuating abilities. Also, the tangential stress can be reduced substantially by about 39.5% through the proper selection of the corresponding material parameters. In addition, this reduction of the tangential stress has a positive effect on the von Mises stress that can be decreased by nearly 33%. Accordingly, the structure would have improved durability and sustain higher loads. These findings would revolutionize the manufacturing of smart structures and enhance their behaviors under severe conditions.

Keywords 2D-FGPMs · Hygrothermal analysis · Rotating disc · Finite element method · Asymmetric loading · Von Mises stress

1 Introduction

Smart materials are becoming more popular than any time before, and their usage is expected to skyrocket due to the inventions of systems replacing humans. They are made of different materials, such as piezoelectric, piezomagnetic, thermoelectric, and morphing materials. This article is concerned with piezoelectrics, which are commonly used in sensing/actuating devices owing to the inherent coupling between their elastic and electric responses. These devices are found in various applications, such as active vibration control systems, marine sonar, energy harvesters, structural health monitoring systems, and medical/aerospace industries. On the other hand, functionally graded piezoelectric materials (FGPMs) are advanced types of piezoelectrics. They have been extensively used in many industries due to their unique characteristics including better durability, performance, and reliability functions compared to homogeneous piezoelectrics [1, 2].

Numerous research articles discussing the performance of the geometrically axisymmetric functionally graded (FG) structures exist in the literature. For example, Jabbari et al. [3, 4] presented solutions for the axisymmetric/asymmetric thermomechanical stresses in cylinders. In Ref. [5], the finite element method (FEM) was used to study the dynamic effects of the heat source, and FG heterogeneity index on the thermoelastic behaviors of cylinders. Similarly, the impacts of the

✉ A. M. Eldeeb
a.eldeeb@m-eng.helwan.edu.eg

Y. M. Shabana
yasser.shabana@gmail.com

A. Elsawaf
elsawaf.ahmed@aast.edu

[1] Mechanical Design Department, Faculty of Engineering, Helwan University, P.O. Box 11718, El-Mataria, Cairo, Egypt

[2] Department of Astronautic Science and Mechanics, Harbin Institute of Technology, Harbin 150001, China

[3] Mechanical Engineering Department, College of Engineering and Technology-Cairo Campus, Arab Academy for Science, Technology and Maritime Transport (AASTMT), Cairo, Egypt

out-of-plane heat flux were examined by Sarkar and Rahman [6] through the finite difference method. That method was also used by Eldeeb and his coauthors to scrutinize the thermoelastoplastic performance of sandwich discs/cylinders [7–9].

In terms of FG piezoelectric structures, authors of Refs. [10–12] developed solutions for the axisymmetric problems of cylinders under different electro-thermo-mechanical boundary conditions (BCs). Wang [13] proposed an approach to predict the thermo-elastic performance of multilayer cylinders with a FG core and homogeneous piezoelectric faces. Wu and Lim [14] assessed the impact of the heterogeneity index, material properties, and BCs on the quasi-three-dimensional dynamic responses of hollow cylinders. In addition, the impacts of asymmetric loads on cylinders were studied in many articles, such as Refs. [15, 16]. Jabbari et al. [2] successively provided a general solution for a porous cylinder under different load configurations using the power series method. Moreover, several authors showed that the presence of moisture has eminent impacts on the resulting stresses of FGPMs [17, 18].

Seeking structures' (e.g., discs) performance improvement, different means are available for that fundamental purpose. Improving the performance means lowering the stresses and raising the yielding limit (higher durability) of any mechanical part. For piezoelectrics, these objectives extend to include enhancing the inherent coupling with the piezoelectric characteristics. Such goals could be achieved through different means that include, but not limited to: parameters' optimization [19], modifying the microstructure to yield a new material with desired properties [20, 21], and developing multi-directional FGMs [22], which is the method used here. In this context, Ghatage et al. [23] indicated that the majority of the studies reported on FG structures are confined to one-dimensional (1D) gradation. Conversely, Nemat-Alla [22] investigated two-dimensional (2D) FGMs and got better performance compared to 1D-FGMs.

Researches on 2D-FGMs are abundantly found in the Cartesian coordinates, see, for example, Refs. [24, 25]. In the polar coordinate system, some articles counted on that idea as a combination of the radial and axial directions [26–31]. On the contrary, limited researches considered simultaneous gradation in the radial and tangential directions, see, for instance, Ref. [32, 33]. Recently, 2D-FG stationary cylinders were examined under nonaxisymmetric thermomechanical loading [34]. The reported results were promising as, for example, mitigations of the tangential and axial stresses were achievable by approximately 63% and 61%, respectively. Therefore, sweeping reductions of the failure probability and/or allowing escalating the severity of the working loads are possible.

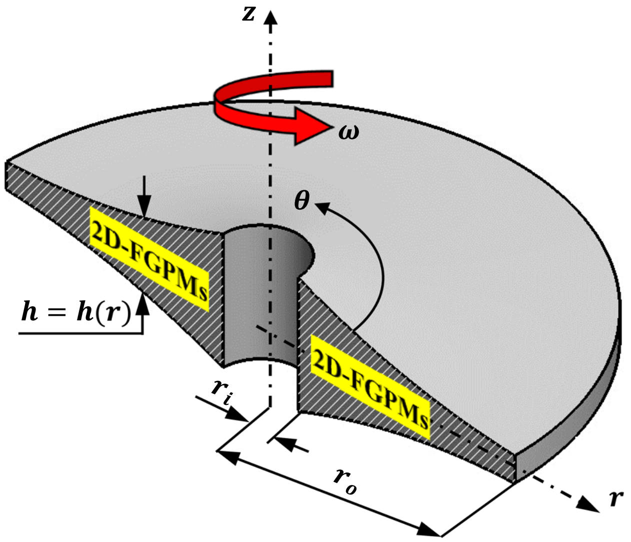

Fig. 1 Configuration of a rotating nonuniform thickness disc. r_i and r_o are the inner and outer radii, respectively. $h(r)$ is a function that describes the thickness h in terms of the radial coordinate r. ω is the angular speed of the disc around the axial coordinate z

In view of the above literature, and to the best of the authors' knowledge, none of the articles considered 2D-FGPMs in the radial and tangential coordinates. Thus, the authors believe that a gap exists in unveiling their performance under complex loading conditions (hygro-thermo-electro-mechanical). Accordingly, this research endeavor aims to examine the potential impacts of applying 2D grading on FGPM sensors/actuators, owing to their profound practical significance. The study delves into the effects of various parameters related to properties grading, exploring their prominent influences on the loading capacity and the sensing/actuating abilities. In this study, these structures are modeled as rotating discs with nonuniform thickness, while being subjected to asymmetric loading conditions. The FEM is employed to solve the differential equations (DEs) governing their behavior.

2 Thickness and Material Formulation

Figure 1 portrays a disc-shaped piezoelectric sensor/actuator in the polar coordinates $(r\theta z)$ with inner and outer radii r_i and r_o, respectively [35].

The disc's thickness ($h = h(r)$) is described according to a power-law formula [36]:

$$h(r) = H\left(1 - n_1\left(\frac{r}{r_o}\right)\right)^{n_2} \tag{1}$$

where r represents the radial coordinate, H is the disc's thickness at $r = 0$, and n_i $(i = 1, 2)$ is a geometrical parameter that governs the disc's profile (e.g., concave, convex, linear, or uniform) [36].

For the material, the disc is made of FGPMs. To model the materials' distribution, gradation in the $r\theta$ plane (θ is the tangential coordinate) is considered to yield 2D-FGPMs. Therefore, any material property (β) is a function of r and θ as follows [34]:

$$\beta(r,\theta)=\beta_i+\left(\frac{\widetilde{\beta}-\widetilde{\beta}_{min}}{\widetilde{\beta}_{max}-\widetilde{\beta}_{min}}\right)(\beta_o-\beta_i) \tag{2}$$

where $\widetilde{\beta}=\beta(r)f(\theta)$ with $f(\theta)$ being a known function in terms of the tangential coordinate θ [32, 33]. Also, the subscripts min and max refer to the minimum and maximum values of $\widetilde{\beta}$, respectively. In addition, $\beta(r)$ is the property that is graded radially according to the following power-law model:

$$\beta(r)=\beta_i+(\beta_o-\beta_i)\left(\frac{r-r_i}{r_o-r_i}\right)^q \tag{3}$$

where q is the heterogeneity index [37].

3 Mathematical Formulation

For a nonuniform thickness disc, the hygro-thermo-electro-mechanical equilibrium equations are [32, 38]:

$$\frac{1}{rh}\left(rh_r\kappa_1M_{,r}\right)_{,r}+\frac{1}{r^2h}(h\kappa_2M)_{,\theta}=0 \tag{4}$$

$$\frac{1}{rh}\left(rh_rk_1T_{,r}\right)_{,r}+\frac{1}{r^2h}(hk_2T)_{,\theta}=0 \tag{5}$$

$$(rh\sigma_{rr})_{,r}+(h\sigma_{r\theta})_{,\theta}-h\sigma_{\theta\theta}+F_r=0 \tag{6}$$

$$(rh\sigma_{r\theta})_{,r}+(h\sigma_{\theta\theta})_{,\theta}+h\sigma_{r\theta}=0 \tag{7}$$

$$\frac{1}{rh}(rhD_r)_{,r}+\frac{1}{r^2h}(h_rD_\theta)_{,\theta}=0 \tag{8}$$

where a comma denotes partial differentiation. M and T are the moisture and temperature, respectively. Also, $\mathbf{k}=\begin{bmatrix}k_1&0\\0&k_2\end{bmatrix}$, and $\boldsymbol{\kappa}=\begin{bmatrix}\kappa_1&0\\0&\kappa_2\end{bmatrix}$ are the thermal conductivity and the moisture diffusivity tensors, respectively. In addition, $\boldsymbol{\sigma}=\left\{\sigma_{rr}\ \sigma_{\theta\theta}\ \sigma_{zz}\ \sigma_{r\theta}\right\}$ is the stress tensor, $\mathbf{D}=\left\{D_r\ D_\theta\right\}$ is the electric displacement, and $F_r=\rho h\omega^2r^2$ is the centrifugal force due to rotation with a constant angular speed ω for a material with a density ρ [8].

On the other hand, the constitutive relations are [38]:

$$\boldsymbol{\sigma}=\mathbf{C}\boldsymbol{\varepsilon}-\mathbf{e}'\mathbf{E}-\boldsymbol{\lambda}T-\boldsymbol{\zeta}M \tag{9}$$

$$\mathbf{D}=\mathbf{e}\boldsymbol{\varepsilon}+\boldsymbol{\mu}\mathbf{E}+\mathbf{p}T+\mathbf{g}M \tag{10}$$

or in the detailed form:

$$\begin{Bmatrix}\sigma_{rr}\\\sigma_{\theta\theta}\\\sigma_{zz}\\\sigma_{r\theta}\end{Bmatrix}=\begin{bmatrix}C_{11}&C_{12}&C_{13}&0\\&C_{22}&C_{23}&0\\&&C_{33}&0\\sym&&&C_{66}\end{bmatrix}\begin{Bmatrix}\varepsilon_{rr}\\\varepsilon_{\theta\theta}\\\varepsilon_{zz}\\2\varepsilon_{r\theta}\end{Bmatrix}-\begin{bmatrix}e_{11}&e_{21}\\e_{12}&e_{22}\\e_{13}&e_{23}\\e_{16}&e_{26}\end{bmatrix}\begin{Bmatrix}E_r\\E_\theta\end{Bmatrix}-\begin{Bmatrix}\lambda_{11}\\\lambda_{22}\\\lambda_{33}\\\lambda_{66}\end{Bmatrix}T-\begin{Bmatrix}\zeta_{11}\\\zeta_{22}\\\zeta_{33}\\\zeta_{66}\end{Bmatrix}M \tag{11}$$

$$\begin{Bmatrix}D_r\\D_\theta\end{Bmatrix}=\begin{bmatrix}e_{11}&e_{12}&e_{13}&e_{16}\\e_{21}&e_{22}&e_{23}&e_{26}\end{bmatrix}\begin{Bmatrix}\varepsilon_{rr}\\\varepsilon_{\theta\theta}\\\varepsilon_{zz}\\2\varepsilon_{r\theta}\end{Bmatrix}+\begin{bmatrix}\mu_{11}&0\\0&\mu_{22}\end{bmatrix}\begin{Bmatrix}E_r\\E_\theta\end{Bmatrix}+\begin{Bmatrix}p_1\\p_2\end{Bmatrix}T+\begin{Bmatrix}g_1\\g_2\end{Bmatrix}M \tag{12}$$

where a prime denotes the transpose of a matrix, $\mathbf{C}=C_{ij}$ (i, $j=1,2,3,6$) represents the elastic stiffness, $\boldsymbol{\mu}=\mu_{ii}$ ($i=1{,}2$) is the dielectric coefficients, and $\mathbf{e}=e_{ij}$ ($i=1{,}2$ and $j=1{,}2{,}3{,}6$) resembles the piezoelectric coefficient matrix. Also, $\mathbf{p}=\left\{p_1\ p_2\right\}$ denotes the pyroelectric coefficient, and $\mathbf{g}=\left\{g_1\ g_2\right\}$ refers to the hygroelectric coefficient. Furthermore, Eq. (13) defines both $\boldsymbol{\lambda}$ and $\boldsymbol{\zeta}$ that are, respectively, the stress-temperature and moisture coefficients [35]:

$$(\lambda,\zeta)=\left(\begin{Bmatrix}\lambda_{11}\\\lambda_{22}\\\lambda_{33}\\\lambda_{66}\end{Bmatrix},\begin{Bmatrix}\zeta_{11}\\\zeta_{22}\\\zeta_{33}\\\zeta_{66}\end{Bmatrix}\right)=\mathbf{C}\left(\begin{Bmatrix}\alpha_1\\\alpha_2\\\alpha_3\\0\end{Bmatrix},\begin{Bmatrix}\gamma_1\\\gamma_2\\\gamma_3\\0\end{Bmatrix}\right) \tag{13}$$

with α_i and γ_i ($i=1,2,3$) are, in turn, the thermal and moisture expansion coefficients.

In Eqs. (11) and (12), the strain and electric fields ($\boldsymbol{\varepsilon}=\left\{\varepsilon_{rr}\ \varepsilon_{\theta\theta}\ \varepsilon_{zz}\ \varepsilon_{r\theta}\right\}$ and $\mathbf{E}=\left\{E_r\ E_\theta\right\}$) are determined as [38]:

$$\varepsilon=\begin{Bmatrix}u_{r,r}\\\left(u_r+u_{\theta,\theta}\right)r^{-1}\\u_{z,z}\\u_{\theta,r}+\left(u_{r,\theta}-u_\theta\right)r^{-1}\end{Bmatrix},\quad\mathbf{E}=\begin{Bmatrix}\phi_{,r}\\r^{-1}\phi_{,\theta}\end{Bmatrix} \tag{14}$$

where u_i ($i=r,\theta,z$) represents the displacement and ϕ is the electric potential.

The above set of relations are valid to be used while considering plane strain conditions. But since the considered disc has $r_o \gg h$, plane stress conditions become more realistic. Thus, σ_{zz} vanishes, leading to reduction of Eqs. (11) and (12) to:

$$\begin{Bmatrix}\sigma_{rr}\\ \sigma_{\theta\theta}\\ \sigma_{r\theta}\end{Bmatrix} = \begin{bmatrix}\widetilde{C}_{11} & \widetilde{C}_{12} & 0\\ & \widetilde{C}_{22} & 0\\ sym & & \widetilde{C}_{66}\end{bmatrix}\begin{Bmatrix}\varepsilon_{rr}\\ \varepsilon_{\theta\theta}\\ 2\varepsilon_{r\theta}\end{Bmatrix} - \begin{bmatrix}\widetilde{e}_{11} & \widetilde{e}_{21}\\ \widetilde{e}_{12} & \widetilde{e}_{22}\\ \widetilde{e}_{16} & \widetilde{e}_{26}\end{bmatrix}\begin{Bmatrix}E_r\\ E_\theta\end{Bmatrix} - \begin{Bmatrix}\widetilde{\lambda}_{11}\\ \widetilde{\lambda}_{22}\\ \widetilde{\lambda}_{66}\end{Bmatrix} T - \begin{Bmatrix}\widetilde{\zeta}_{11}\\ \widetilde{\zeta}_{22}\\ \widetilde{\zeta}_{66}\end{Bmatrix} M \tag{15}$$

$$\begin{Bmatrix}D_r\\ D_\theta\end{Bmatrix} = \begin{bmatrix}\widetilde{e}_{11} & \widetilde{e}_{12} & \widetilde{e}_{16}\\ \widetilde{e}_{21} & \widetilde{e}_{22} & \widetilde{e}_{26}\end{bmatrix}\begin{Bmatrix}\varepsilon_{rr}\\ \varepsilon_{\theta\theta}\\ 2\varepsilon_{r\theta}\end{Bmatrix} + \begin{bmatrix}\widetilde{\mu}_{11} & \widetilde{\mu}_{12}\\ \widetilde{\mu}_{21} & \widetilde{\mu}_{22}\end{bmatrix}\begin{Bmatrix}E_r\\ E_\theta\end{Bmatrix} + \begin{Bmatrix}\widetilde{p}_1\\ \widetilde{p}_2\end{Bmatrix} T + \begin{Bmatrix}\widetilde{g}_1\\ \widetilde{g}_2\end{Bmatrix} M \tag{16}$$

where $\widetilde{\beta}$ is the corresponding value of any β for the plane stress conditions given in Eq. (A–1) in Appendix (A).

4 Numerical Solution

Within the current study, the solution of the DEs is executed through the FEM due its features in solving such complicated systems [5]. In general, the FEM solves for the unknowns' vector $\mathbf{X} = \begin{Bmatrix} U & \phi & M & T \end{Bmatrix}$ with $U = \begin{Bmatrix} u_r & u_\theta \end{Bmatrix}$, as follows [39]:

$$\mathbf{X} \approx \sum_{i=1}^{n_n} N_i^j \mathbf{X}_i \tag{17}$$

where N is the shape function and X_i is the unknown value at the ith node of the jth element that is composed of number of nodes n_n.

Moreover, for a system consisting of total number of elements n_e, the subsequent symbolic representation is written after applying the FE solution procedures [39]:

$$\sum_{j=1}^{n_e}\left(\begin{bmatrix}\mathbf{K}_{\mathrm{UU}}^j & \mathbf{K}_{\mathrm{U}\phi}^j & \mathbf{K}_{\mathrm{UM}}^j & \mathbf{K}_{\mathrm{UT}}^j\\ \mathbf{K}_{\phi\mathrm{U}}^j & \mathbf{K}_{\phi\phi}^j & \mathbf{K}_{\phi\mathrm{M}}^j & \mathbf{K}_{\phi\mathrm{T}}^j\\ 0 & 0 & \mathbf{K}_{\mathrm{MM}}^j & 0\\ 0 & 0 & 0 & \mathbf{K}_{\mathrm{TT}}^j\end{bmatrix}\begin{Bmatrix}U^j\\ \phi^j\\ M^j\\ T^j\end{Bmatrix} = \begin{Bmatrix}\mathbf{R}_{\mathrm{U}}^j\\ 0\\ 0\\ 0\end{Bmatrix}\right) \tag{18}$$

where $\mathbf{K}^j$ and $\mathbf{R}^j$ are the stiffness matrix and force vector, respectively, for the jth element. Further details regarding them could be found in Appendix (B). As a final step after having the vector $\mathbf{X}$ at each node using matrix calculus, both $\boldsymbol{\varepsilon}$ and $\boldsymbol{\sigma}$ are evaluated directly while enforcing the BCs [39].

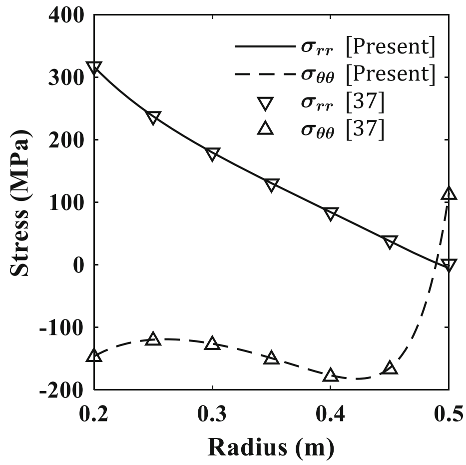

Fig. 2 Current FEM stresses against those of Ref. [37] at $\theta = 0°$

5 Solution Scheme Justification

In this section, the authors justify the ability of the proposed solution algorithm and the developed MATLAB code through regenerating the results of three examples from the literature.

The first example is a 1D-FGM nonuniform thickness disc studied by Hassani et al. [37]. It has $r_i = 0.2$m, $r_o = 0.5$m, $h(r) = 0.05(r/r_o)^{0.3}$, $\omega = 500$rad/s and is prone to the following symmetric (independent of θ) BCs [37]:

$$u_r(r_i) = u_\theta(r_i) = 0 \tag{19}$$

$$\sigma_{rr}(r_o) = \sigma_{r\theta}(r_o) = 0 \tag{20}$$

$$T(r) = 150 + (400 - 150)\left(\frac{r_i - r}{r_i - r_o}\right)(°\mathrm{C}) \tag{21}$$

The material properties used in this example are explicitly stated in Ref. [37] and are radially graded according to Eq. (3) with $q = 5$. Figure 2 depicts the distribution of stresses produced by the current FE solution and by Hassani et al. [37].

The second justification example to be regenerated considers a nonrotating circular annulus studied by Chawde and Bhandakkar [40]. It was assumed that the annulus has $r_i = 0.5r_o$, and $h(r) = 1$. It was made of isotropic FGM with Poisson's ratio $\upsilon = 1/3$, and shear modulus $G(r) = \frac{3}{8}(r/r_o)^2$ [40]. Under the plane stress conditions, the following mixed

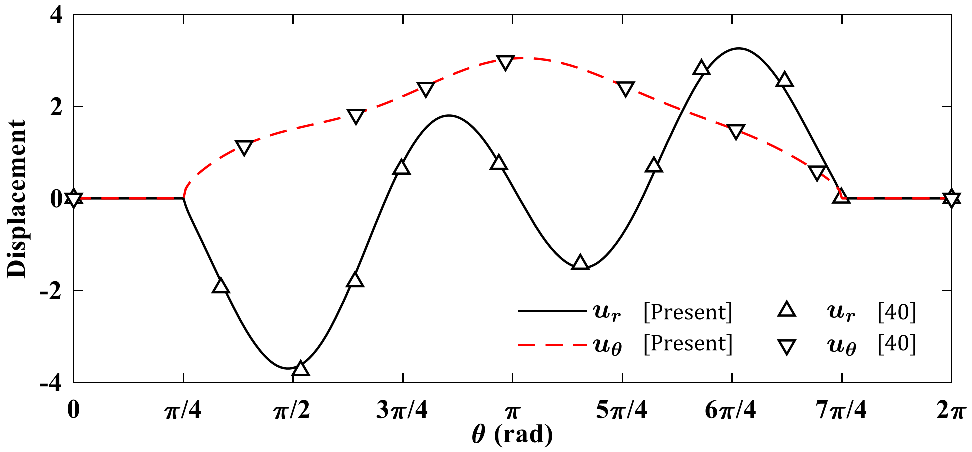

Fig. 3 Angular distributions of the displacements obtained through FEM and by Ref. [40] at $r = r_o$

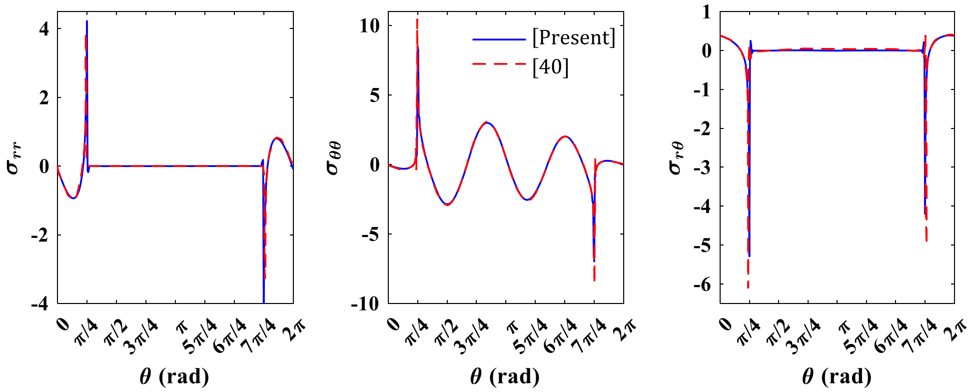

(a) (b) (c)

Fig. 4 Angular distributions of the stresses obtained through FEM and by Ref. [40] at $r = r_o$. **a** σ_{rr}, **b** $\sigma_{\theta\theta}$, and **c** $\sigma_{r\theta}$

BCs were used:

$$\begin{array}{ll}\left.\begin{aligned}\sigma_{rr}(r_i,\theta)&=-\sin(3\theta)-\cos(2\theta)\\ \sigma_{r\theta}(r_i,\theta)&=-\cos(3\theta)-\sin(2\theta)\end{aligned}\right\} & 0\le\theta\le 2\pi\\ \left.\begin{aligned}u_r(r_o,\theta)&=0\\ u_\theta(r_o,\theta)&=0\end{aligned}\right\} & -\frac{\pi}{4}\le\theta\le\frac{\pi}{4}\\ \left.\begin{aligned}\sigma_{rr}(r_o,\theta)&=0\\ \sigma_{r\theta}(r_o,\theta)&=0\end{aligned}\right\} & \frac{\pi}{4}<\theta<\frac{7\pi}{4}\end{array}\tag{22}$$

The distributions of both u and $\boldsymbol{\sigma}$ at $r = r_o$ using the two methodologies are depicted in Figs. 3 and 4, respectively. It is noticed that the results are in a great match. However, owing to the excessively large value of the stress components (Fig. 4) at the singular points ($r = r_o, \theta = \pm\pi/4$), there are some differences for $\boldsymbol{\sigma}$, and this is satisfactory as Ref. [40] presented.

The final example provides proof of the ability of the current analyses to handle piezoelectric problems. A piezoelectric cylinder investigated by Galic and Horgan [41] is re-examined. It has $r_i = r_o/4$ and made of PZT-4 (Table 1 in Ref. [41] defines the material properties). Under the plane strain state, the cylinder has a rotating speed $\omega = \left(C_{11}/r_i^2\rho\right)^{1/2}$ with the following axisymmetric BCs: $\sigma_{rr}(r_i) = \sigma_{rr}(r_o) = 0$, $\phi(r_i) = r_i C_{11}/e_{11}$, and $\phi(r_o) = 0$. The resulting dimensionless $\boldsymbol{\sigma}$ and ϕ are depicted in Fig. 5, where the results of the developed FE scheme are in great agreement with those obtained in Ref. [41].

Based on the outcomes of these validation examples, there is a significant consistency between the obtained FE results and those of the verified references. This demonstrates the reliability of the formulation and coding in solving similar problems efficiently.

6 Results and Discussion

In the framework of this study, a FE scheme is built through the MATLAB software to investigate the performance of FGPM sensor/actuator. For FEM, $n_e = 15000$ element of the type isoparametric two-dimensional quadrilateral element with $n_n = 8$. In detail, n_e is divided into $n_{e_r} = 100$ and $n_{e_\theta} = 150$ elements along r and θ directions, respectively. Also, a complete integration is executed over the element with nine gauss points. Appendix (B) presents additional information regarding FEM, including a schematic drawing for the mesh and the element with its corresponding N.

Table 1 Properties of PZT-4 and $Ba_2NaNb_5O_{15}$ [14, 43–45]

Material	Elastic constants (GPa)							
	C_{11}	$C_{12} = C_{13}$	C_{22}	C_{33}	$C_{23} = C_{32}$	C_{44}	C_{55}	C_{66}
PZT-4	115	74	139	139	78	30.5	25.6	25.6
$Ba_2NaNb_5O_{15}$	135	74	247	239	104	76	66	66

	Piezoelectric constants (C/m^2)				Dielectric permittivity ($10^{-9} \times C^2/Nm^2$)		Density (kg/m^3)
	e_{11}	e_{12}	e_{13}	$e_{26} = e_{35}$	μ_{11}	$\mu_{22} = \mu_{33}$	ρ
PZT-4	15.1	−5.2	−5.2	12.7	5.6	6.5	7500
$Ba_2NaNb_5O_{15}$	4.3	−0.3	−0.4	2.8	0.28	1.96	5300

	Thermal expansion (10^{-6}/°C)		Moisture expansion ($10^{-5} \times m^3/kg$)		Pyroelectric constants ($10^{-5} \times C/m^2K$)	
	α_1	$\alpha_2 = \alpha_3$	γ_1	$\gamma_2 = \gamma_3$	p_1	$p_2 = p_3$
PZT-4	20	2	8	11	5.4	0
$Ba_2NaNb_5O_{15}$	2.45	4.39	8	16	5.4	0

	Moisture diffusion coefficient ($10^{-10} \times m^2/s$)	Thermal conductivity (W/mK)		Hygroelectric coefficient ($10^{-5} \times Cm/kg$)	
	$\kappa_1 = \kappa_2 = \kappa_3$	k_1	$k_2 = k_3$	g_1	$g_2 = g_3$
PZT-4	4.3	2.5	2.1	−2.5	0
$Ba_2NaNb_5O_{15}$	17.31	13.9	8.6	−2.5	0

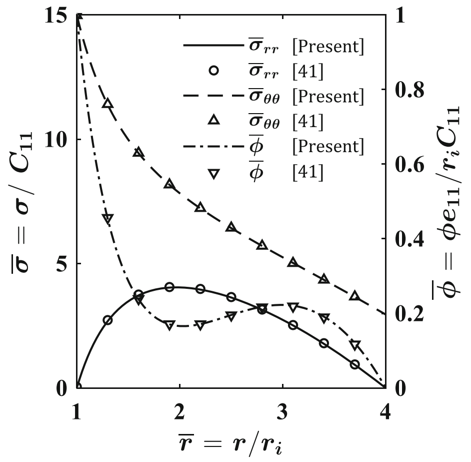

Fig. 5 Dimensionless distribution of the stresses and electric potential obtained through FEM and Ref. [41]

On the other hand, the circular sensor/actuator is modeled as a disc with $r_o = 0.5\text{m} = 2r_i$ [35]. It rotates with $\omega = 500\text{rad/s}$, and has a concave thickness profile described by Eq. (1) with the following values: $H = 0.1\text{m}$, $n_1 = 0.4151965$ and $n_2 = 3$ [36, 42].

Concerning material properties, they are graded radially according to Eq. (3) with $q = 1$ from PZT-4 at $r = r_i$ to $Ba_2NaNb_5O_{15}$ at $r = r_o$. Table 1 lists the material properties used in the current analysis [14, 43–45].

Afterward, a trigonometric $f(\theta)$ is used to grade the material tangentially, such that

$$f(\theta) = \cos(n_\theta \theta + \psi) \quad (23)$$

where n_θ (angular coefficient) and ψ (shifting angle) are two independent parameters [34]. Here, the analysis is limited to $n_\theta = 1$ and 2 as examples to examine the idea itself.

As presented in Sect. 1, the use of 2D material gradation was proven to be advantageous for FGM structures from the stresses viewpoint for FGM structures [34]. However, this idea has not been applied to circular FGPM ones in the $r\theta$ plane.

Before discussing the results, three points are important to be mentioned. (i) All the stresses calculated through this section are presented in a dimensionless form, such that $\bar{\sigma} = \sigma / P^*$ with $P^* = 100\text{MPa}$. (ii) The von Mises stress (σ_{VM}) is calculated to assess the disc's failure probability and load capacity. It is obtained according to Eq. (24), and presented

Table 2 Mathematical expressions of the BCs

Inner surface	Outer surface
$u_r(\theta) = u_\theta(\theta) = 0$	$\sigma_{rr}(0^\circ \le \theta \le 45^\circ) = 5P^*\cos(2\theta)$
$\phi(\theta) = 0$	$\phi(45^\circ \le \theta \le 90^\circ) = \phi_0 \sin(\theta)$
$T(\theta) = T_0 + 50\sin(\theta)^\circ\text{C}$	$T(\theta) = 50^\circ\text{C}$
$M(\theta) = 25 + 5\cos(\theta)\text{kg/m}^3$	$M(\theta) = 0$

Table 3 Selected maximum and/or minimum values of a 1D-FGPM disc

Quantity	Value	Quantity	Value
$u_{r_{max}}$	1.979mm	$\bar{\sigma}_{VM_{max}}$	7.2
$\bar{\sigma}_{\theta\theta_{max}}$	3.66	$\bar{\sigma}_{\theta\theta_{min}}$	−8.24

in a dimensionless form ($\bar{\sigma}_{VM} = \sigma_{VM}/P^*$) [34].

$$\sigma_{\text{VM}} = \left(\sigma_{rr}^2 - \sigma_{rr}\sigma_{\theta\theta} + \sigma_{\theta\theta}^2 + 3\sigma_{r\theta}^2\right)^{1/2} \tag{24}$$

(iii) The authors focused on u_r, $\bar{\sigma}_{\theta\theta}$ and $\bar{\sigma}_{VM}$ to judge on the performance. The first affects mainly the function as a sensor or actuator. The second is a stress component that has been considered by many authors to be more critical if compared to σ_{rr} and $\sigma_{r\theta}$; thus, they are neglected. The third identifies the failure likelihood and the loading capacity of the structure.

By moving to the results, a smart structure modeled as a disc placed in a hygrothermal environment (simulates a real situation of working conditions, especially for applications in hot/humid areas and near coast ones). The BCs used are listed in Table 2 with $\phi_0 = 500$V, $n_p = 2$ (pressure frequency), and $n_\phi = 1$ (potential frequency).

The results of a 1D-FGPM disc (Eq. 3) are presented in Figs. 6 and 7. Some of the maximum/minimum values are listed in Table 3. Then, the results of using 2D-FGPMs (Eq. 2) are displayed. Figure 8 shows the distribution of T and M at

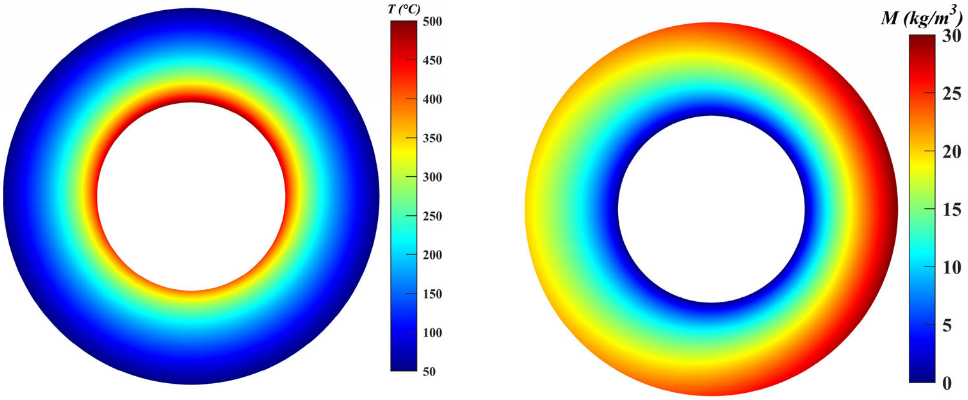

(a) T (b) M

Fig. 6 Distribution of **a** T and **b** M of a 1D-FGPM disc ($f(\theta) = 1$)

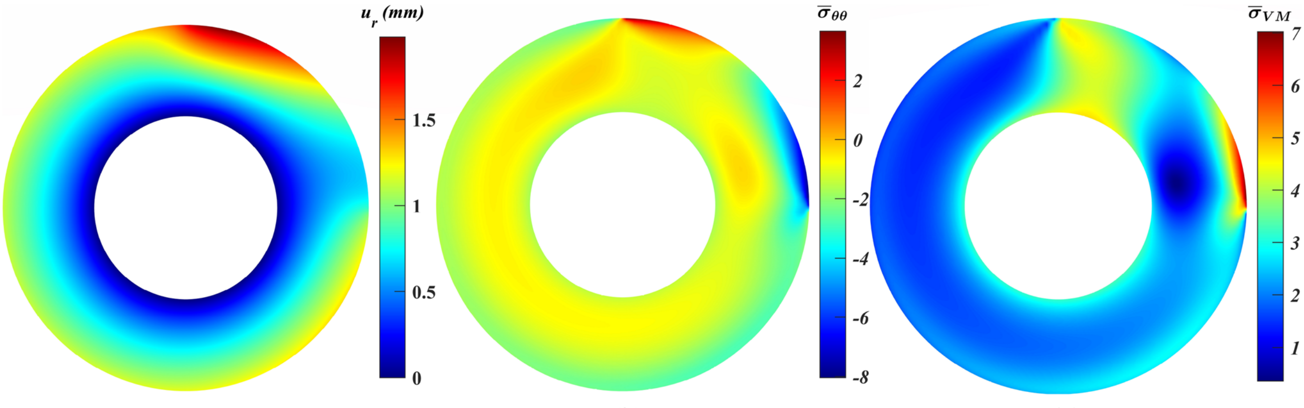

(a) u_r (b) $\bar{\sigma}_{\theta\theta}$ (c) $\bar{\sigma}_{VM}$

Fig. 7 Distributions of **a** u_r, **b** $\bar{\sigma}_{\theta\theta}$, and **c** $\bar{\sigma}_{VM}$ of a 1D-FGPM disc ($f(\theta) = 1$)

Fig. 8 Distributions of T and M of a 2D-FGPM disc at different values of $f(\theta)$

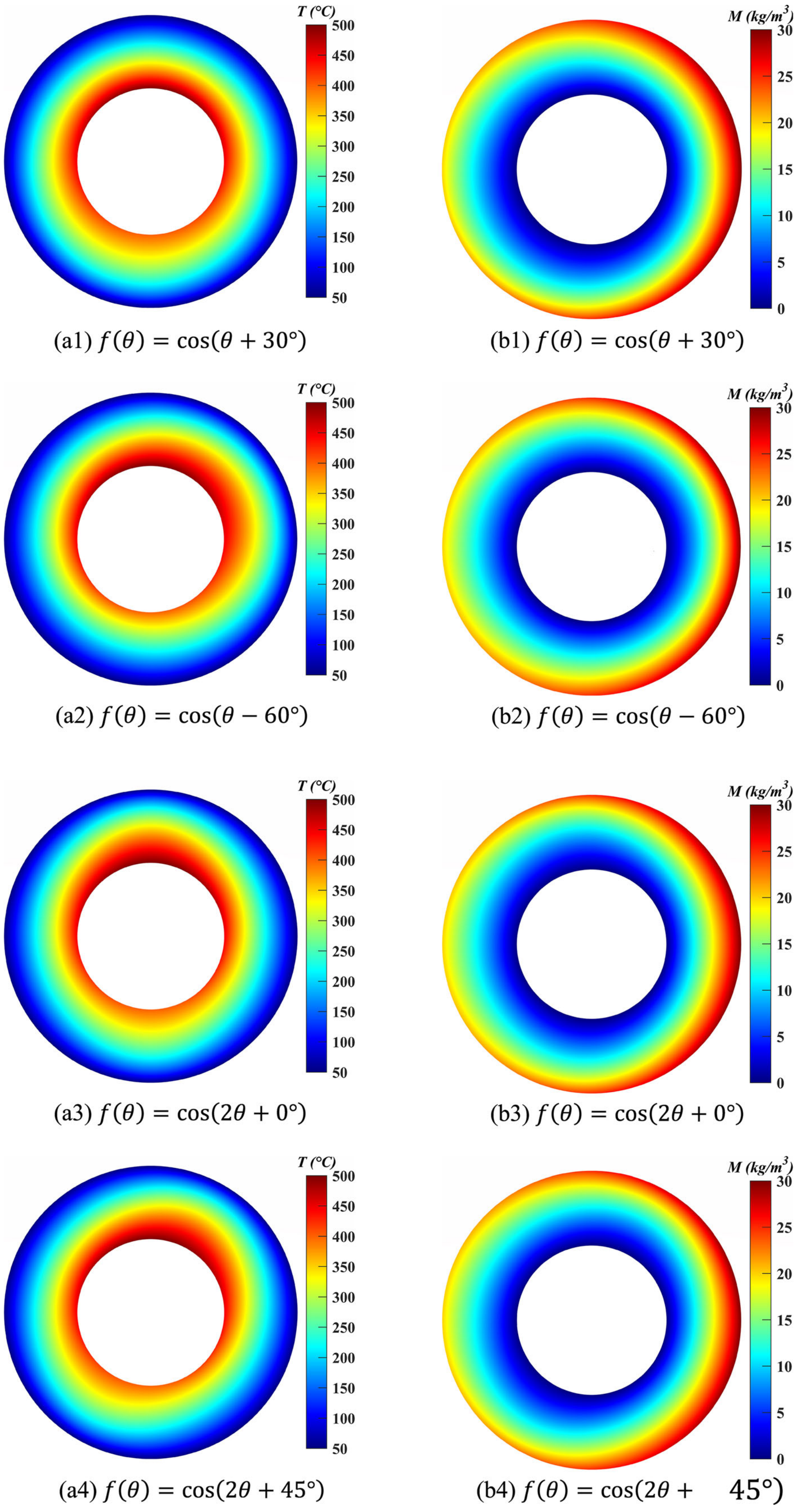

(a1) $f(\theta) = \cos(\theta + 30°)$ (b1) $f(\theta) = \cos(\theta + 30°)$

(a2) $f(\theta) = \cos(\theta - 60°)$ (b2) $f(\theta) = \cos(\theta - 60°)$

(a3) $f(\theta) = \cos(2\theta + 0°)$ (b3) $f(\theta) = \cos(2\theta + 0°)$

(a4) $f(\theta) = \cos(2\theta + 45°)$ (b4) $f(\theta) = \cos(2\theta + 45°)$

Fig. 9 Radial distribution of (**a**) T and (**b**) M at $\theta = 0°$ for different values of $f(\theta)$

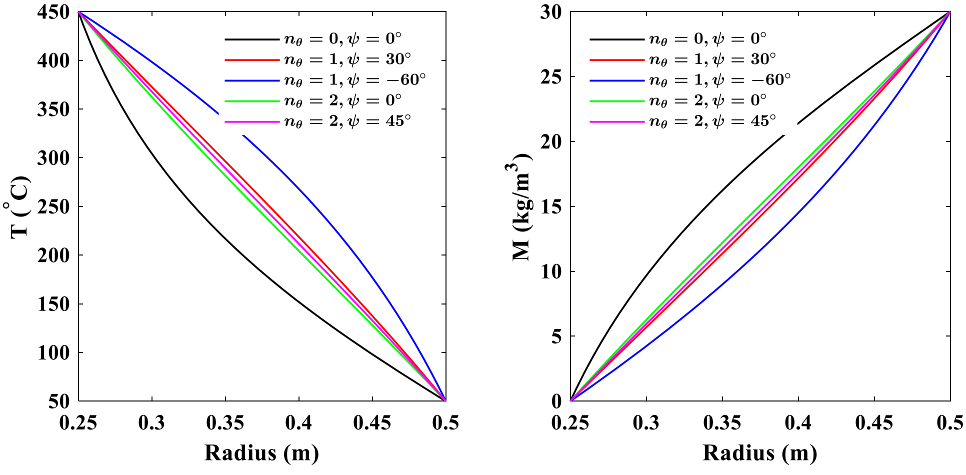

(a) (b)

Fig. 10 Distributions of u_r for a 2D-FGPM disc. **a** $n_\theta = 1$ and $\psi = 30°$, **b** $n_\theta = 1$ and $\psi = -60°$, **c** $n_\theta = 2$ and $\psi = 0°$, and **d** $n_\theta = 2$ and $\psi = 45°$

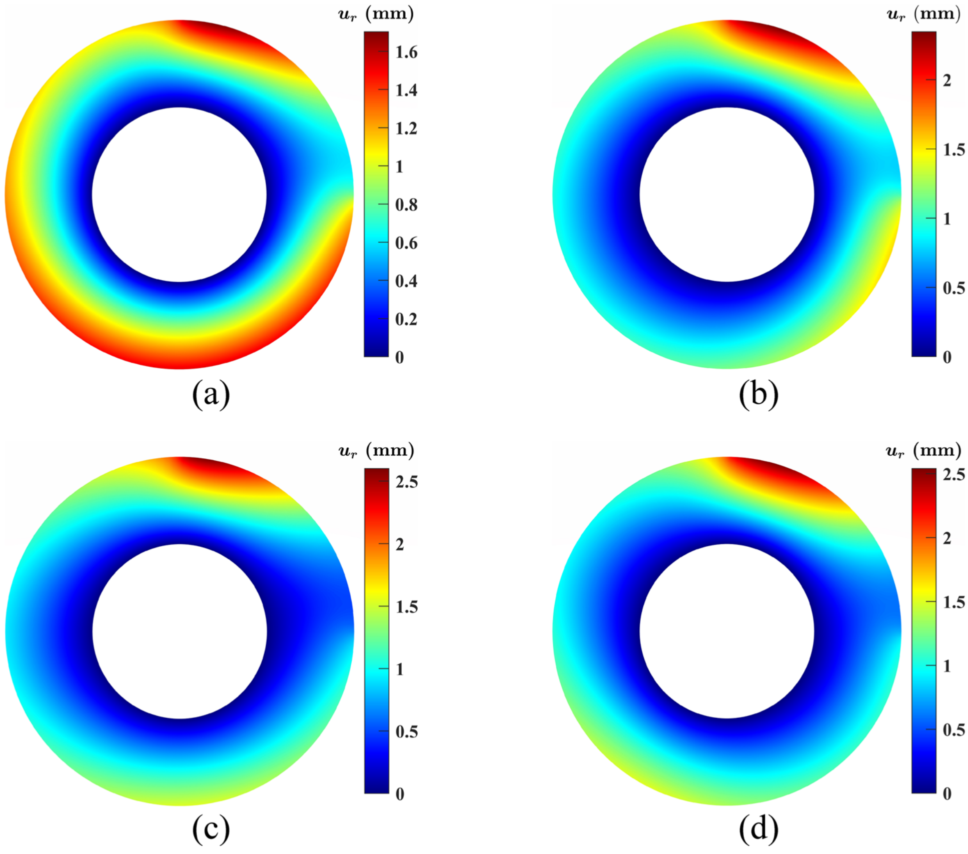

the selected values of n_θ and ψ. Also, the corresponding u_r, $\bar{\sigma}_{\theta\theta}$ and $\bar{\sigma}_{VM}$ are depicted in Figs. 10, 12 and 13, respectively.

As seen in Fig. 8, the extreme values of T and M remained unchanged and occur at the boundaries. In contrast, their intermediate values witnessed some variations with opposing behaviors, which can be seen in Fig. 9 at $\theta = 0°$, where it is evident that T increased with a reduction of M.

In terms of u_r, different trends are noticed. Scrutinizing Fig. 10a reveals that $u_{r_{max}}$ declined by $\sim$ 13.9% at $n_\theta = 1$ and $\psi = 30°$ compared to the maximum value listed in Table 3. On the other hand, it increased by almost 19% by using $\psi = -60°$ (Fig. 10b). This percentage grew to hit approximately 31% and 28.3% at $\psi = 0°$ (Fig. 10c) and 45° (Fig. 10d), respectively, while grading the material properties with $n_\theta = 2$.

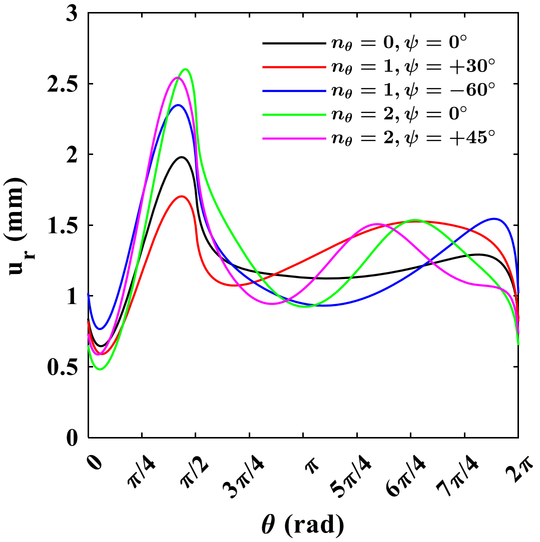

Fig. 11 Angular distribution of u_r at the outer circumference

Therefore, it can be emphasized that using 2D-FGPMs would raise the displacement in most cases of n_θ and ψ as seen in Fig. 11. This is vital for structures performing either as sensors or as actuators. For the former, this is essential to raise their sensitivity, and become able to read tiny signals. On the other hand, an actuator can make use of larger or smaller displacements depending on the required function. Thus, from u_r viewpoint, 2D-FGPM is highly beneficial.

Concerning $\bar{\sigma}_{\theta\theta}$, it experienced fundamental changes leading to drastic modifications to $\bar{\sigma}_{VM}$ as to be shown later. In more detail, Fig. 12a depicts that the maximum tensile $\bar{\sigma}_{\theta\theta}$ went down by almost 39.5% at $n_\theta = 1$ and $\psi = 30°$ in contrast to their value at $f(\theta) = 1$ (Fig. 7b and Table 3). Conversely, there was a substantial growth at $\psi = -60°$ by nearly 23.8% (Fig. 12b). That growth increased by around 33% (Fig. 12c) and 5% (Fig. 12d) at $\psi = 0°$ and 45°, respectively, while n_θ was adjusted to 2. In the same vein, $\bar{\sigma}_{\theta\theta_{min}}$ has similar counteractive trends as of $\bar{\sigma}_{\theta\theta_{max}}$. Originally, it stood at -8.24 (Fig. 7b and Table 3); then, upon applying 2D gradation, it declined moderately by $\sim$ 19% at $n_\theta = 1$ and $\psi = 30°$. Further decrease reaching almost threefold of the previous percentage was applicable by using $\psi = -60°$ (Fig. 12b). Moreover, $\bar{\sigma}_{\theta\theta_{min}}$ declined by a faire percentage ($\sim$ 15.4%) at $\psi = 45°$ (Fig. 12d). Conversely, Fig. 12c depicts that at $n_\theta = 2$ and $\psi = 0°$, $\bar{\sigma}_{\theta\theta_{min}}$ rose up, but with a less percentage compared to that of $\bar{\sigma}_{\theta\theta_{max}}$.

Fig. 12 Distributions of $\bar{\sigma}_{\theta\theta}$ for a 2D-FGPM disc. **a** $n_\theta = 1$ and $\psi = 30°$, **b** $n_\theta = 1$ and $\psi = -60°$, **c** $n_\theta = 2$ and $\psi = 0°$, and **d** $n_\theta = 2$ and $\psi = 45°$

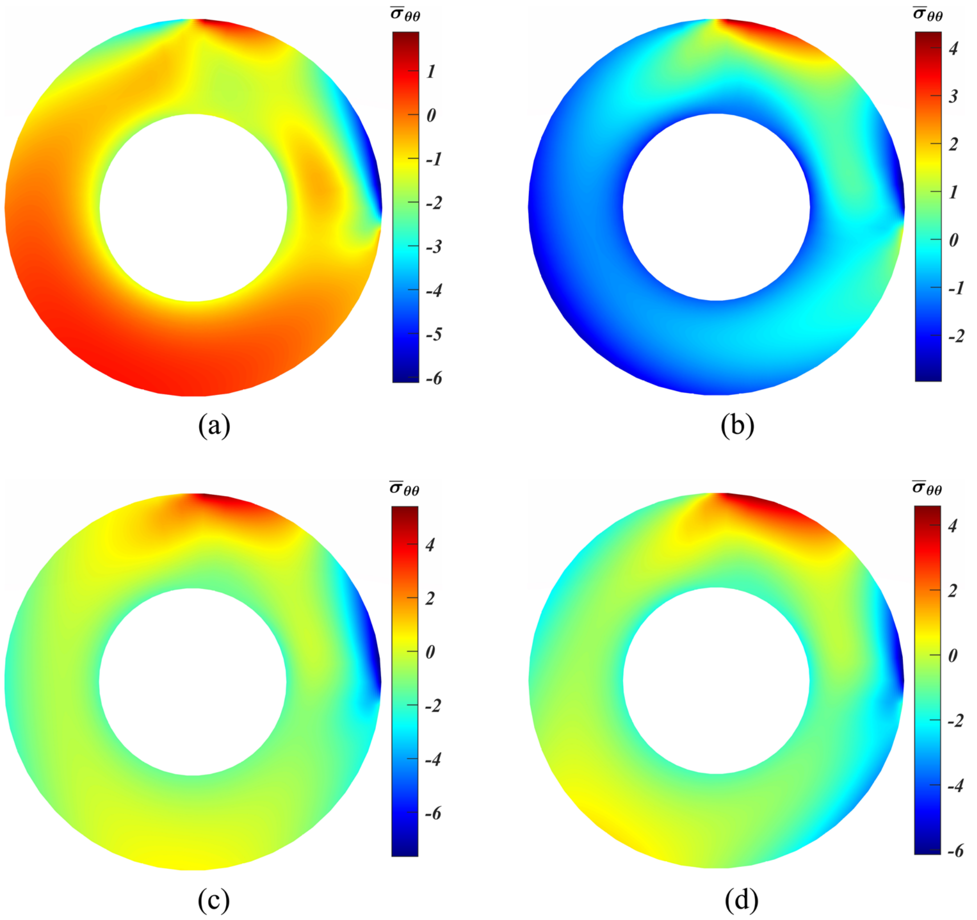

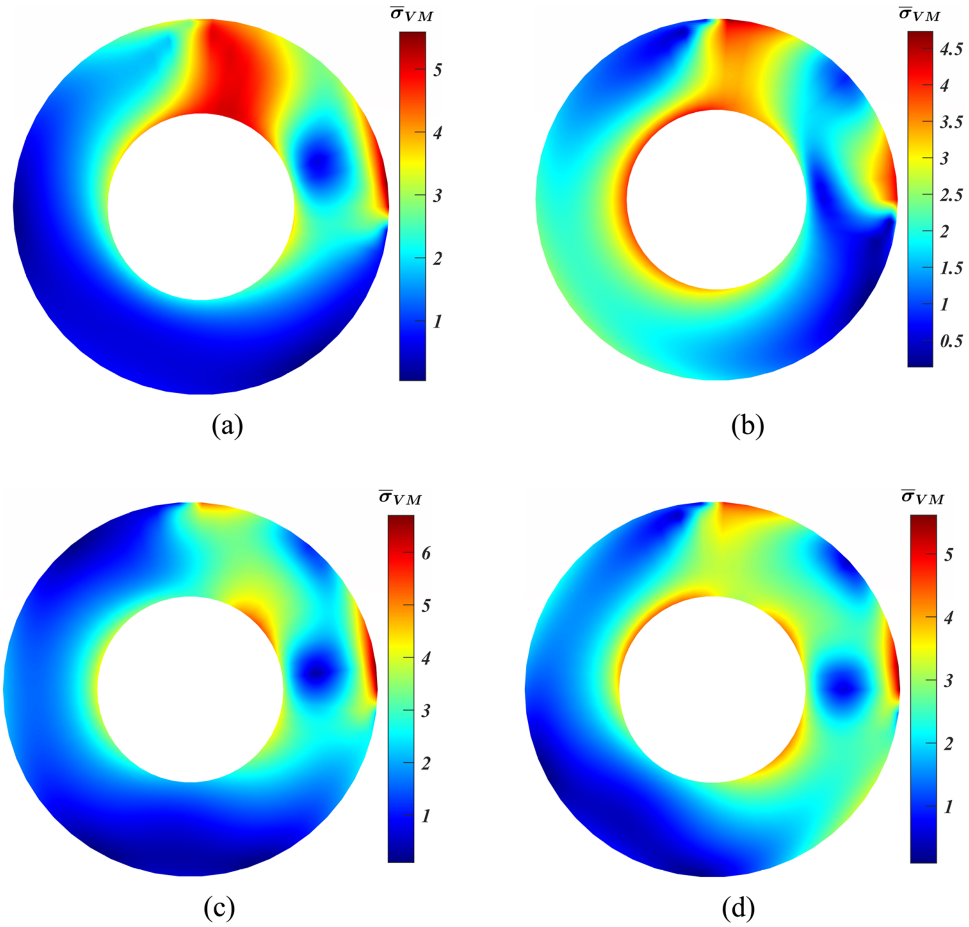

(a) (b)

(c) (d)

Fig. 13 Distributions of $\bar{\sigma}_{VM}$ for a 2D-FGPM disc. **a** $n_\theta = 1$ and $\psi = 30°$, **b** $n_\theta = 1$ and $\psi = -60°$, **c** $n_\theta = 2$ and $\psi = 0°$, and **d** $n_\theta = 2$ and $\psi = 45°$

By moving to $\bar{\sigma}_{VM}$, its values and distributions are impacted deterministically by the radical variations occurred to $\bar{\sigma}_{\theta\theta}$. In general, $\bar{\sigma}_{VM_{max}}$ declined by $\sim 16.4\%$ as a logical consequence to the reductions occurred to $\bar{\sigma}_{\theta\theta}$ when $n_\theta = 1$ and $\psi = 30°$ as shown in Fig. 13a. Interestingly, that percentage continued to grow reaching almost its double when $\psi = -60°$ (Fig. 13b) despite the considerable escalation that occurred to $\bar{\sigma}_{\theta\theta_{max}}$, which is similar to what is noticed at $n_\theta = 2$ and $\psi = 45°$ (Fig. 13d). On the contrary and as expected, $\bar{\sigma}_{VM_{max}}$ experienced a slight increase by nearly 3% at $n_\theta = 2$ and $\psi = 0°$ due to the augmentation happened to $\bar{\sigma}_{\theta\theta}$ as seen in Fig. 13c.

Accordingly, it can be deduced that 2D-FGPM discs pose enhanced performance compared to 1D-FGPM ones in terms of reducing the failure probability, raising the loading capacity, and, in some cases, improving the function role as sensors/actuators. Furthermore, the variations of the results are dependent on the constituent material properties, geometry, and loading status. Additionally, the two independent parameters of Eq. (23) have profound impacts on the performance trends. Therefore, they should be chosen carefully.

7 Conclusion

In this study, sensors/actuators were modeled as variable thickness discs made of FGPMs. The material properties were assumed to be graded concurrently in the radial and tangential directions developing 2D-FGPMs. The finite element method was used to solve the problem and obtain the hygrothermoelectroelastic behaviors. Results obtained were promising, and the main ones are highlighted as follows:

- 2D grading of the material properties affected the displacement pattern significantly compared to 1D-FGPMs. This is highly beneficial for both the sensing and actuating abilities.
- The consideration of 2D material distribution led to counteractive behaviors of both the temperature and moisture distributions in contrast to 1D-FGPM disc. However, their upper and lower values did not encounter changes.
- 2D material gradation, in most cases, would yield smaller tangential stress compared to the conventional 1D-FGPMs. For example, around 39.5% reduction was attained for the maximum compressive tangential stress.

- The maximum loads that the proposed disc could sustain could be increased due to the attainable reductions of the von Mises stress that could reach approximately 33%.
- Performing an adequate optimization process of the working parameters is essential to highly enhance the performance at certain working conditions.

Funding Open access funding provided by The Science, Technology & Innovation Funding Authority (STDF) in cooperation with The Egyptian Knowledge Bank (EKB). This research did not receive any specific grant from funding agencies in the public, commercial, or not-for-profit sectors.

Data availability The raw/processed data required to reproduce these findings cannot be shared at this time as the data also form part of an ongoing study.

Declarations

Conflict interest The author(s) declared no potential conflicts of interest with respect to the research, authorship, and/or publication of this article.

Appendix: Plane Strain/Stress Transformation

In this part, the authors would like to present the switching formulae of the material properties from the plane strain state to the plane stress conditions. β signifies the plane strain property, and $\widetilde{\beta}$ stands for its corresponding property at the plane stress state.

$$\left.\begin{array}{ll} \widetilde{C}_{ij} = C_{ij} - \frac{C_{i3}C_{j3}}{C_{33}} & \widetilde{e}_{ij} = e_{ij} - \frac{C_{j3}e_{i3}}{C_{33}} \\ \widetilde{\mu}_{ii} = \mu_{ii} + \frac{e_{i3}e_{13}}{C_{33}} & \widetilde{e}_{i6} = e_{i6} \\ \widetilde{\lambda}_{ii} = \lambda_{ii} + \frac{C_{i3}\lambda_{33}}{C_{33}} & \widetilde{\zeta}_{ii} = \zeta_{ii} + \frac{C_{i3}\zeta_{33}}{C_{33}} \\ \widetilde{p}_{i} = p_{i} + \frac{e_{i3}\lambda_{33}}{C_{33}} & \widetilde{g}_{i} = g_{i} + \frac{e_{i3}\zeta_{33}}{C_{33}} \end{array}\right\} i,\ j = 1,\ 2$$
$$\widetilde{C}_{66} = C_{66}\ \ \widetilde{\mu}_{ij} = \frac{e_{i3}e_{23}}{C_{33}} \rightarrow i,\ j = 1,\ 2 \text{ and } i \neq j \tag{A–1}$$

Appendix B: FEM Expansion

Within the framework of this study, the FEM is used. There are multiple types of two-dimensional elements to be used, such as the three-/six-node triangular elements and the four-/eight-node quadrilateral elements. The authors developed a MATLAB code so as to mesh the domain using the quadrilateral elements.

In this study, the eight-node ($n_n = 8$) isoparametric two-dimensional quadrilateral element is used for its improved level of accuracy that requires a smaller number of elements compared to the four-node element. Figure (B–1) shows a hypothetical mesh for the disc's domain with a schematic drawing of the used eight-node element and the corresponding locations of the gauss points [39].

The shape function at the i^{th} node of such element is expressed as [39]:

$$\left.\begin{array}{rl} N_i(\xi_i, \eta_i) = \frac{1}{4}(1+\xi\xi_i)(1+\eta\eta_i)(\xi\xi_i+\eta\eta_i-1) & \rightarrow i = 1, .., 4 \\ N_i(0, \eta_i) = \frac{1}{2}\left(1-\xi^2\right)(1+\eta\eta_i) & \rightarrow i = 5, 7 \\ N_i(\xi_i, 0) = \frac{1}{2}(1+\xi\xi_i)\left(1-\eta^2\right) & \rightarrow i = 6, 8 \end{array}\right\} \tag{B–1}$$

It is important to mention that the natural coordinates of the element vary as $-1 \leq (\xi_i, \eta_i) \leq +1$.

Concerning the terms of Eq. (18), they are determined as follows:

$$\mathbf{K}^j_{\mathrm{UU}} = \int_{\Omega_e} rh[\mathbf{B}_{\mathrm{U}}]'\left[\widetilde{\mathbf{C}}\right][\mathbf{B}_{\mathrm{U}}]\mathrm{d}\Omega_e$$
$$\mathbf{K}^j_{\phi\phi} = -\int_{\Omega_e} rh\left[\mathbf{B}_\phi\right]'[\widetilde{\mu}]\left[\mathbf{B}_\phi\right]\mathrm{d}\Omega_e \tag{B–2}$$
$$K^j_{\mathrm{UT}} = -\int_{\Omega_e} rh[\mathbf{B}_{\mathrm{U}}]'\left[\widetilde{\lambda}\right][\mathbf{N}]\mathrm{d}\Omega_e$$
$$\mathbf{K}^j_{\mathrm{UM}} = -\int_{\Omega_e} rh[\mathbf{B}_{\mathrm{U}}]'\left[\widetilde{\zeta}\right][\mathbf{N}]\mathrm{d}\Omega_e$$
$$\mathbf{K}^j_{\phi\mathrm{M}} = \int_{\Omega_e} rh\left[\mathbf{B}_\phi\right]'\left[\widetilde{\mathbf{g}}\right][\mathbf{N}]\mathrm{d}\Omega_e\ \mathbf{K}^j_{\phi\mathrm{T}} = \int_{\Omega_e} rh\left[\mathbf{B}_\phi\right]'\left[\widetilde{\mathbf{p}}\right][\mathbf{N}]\mathrm{d}\Omega_e$$
$$\mathbf{K}^j_{\mathrm{U}\phi} = \int_{\Omega_e} rh[\mathbf{B}_{\mathrm{U}}]'[\widetilde{\mathbf{e}}]'\left[\mathbf{B}_\phi\right]\mathrm{d}\Omega_e\ \mathbf{K}^j_{\phi\mathrm{U}} = \int_{\Omega_e} rh\left[\mathbf{B}_\phi\right]'[\widetilde{\mathbf{e}}][\mathbf{B}_{\mathrm{U}}]\mathrm{d}\Omega_e$$
$$\mathbf{K}^j_{\mathrm{MM}} = \int_{\Omega_e} rh[\mathbf{B}_{\mathrm{M}}]'[\kappa][\mathbf{B}_{\mathrm{M}}]\mathrm{d}\Omega_e$$
$$\mathbf{R}^j_{\mathrm{U}} = \int_{\Gamma} rh[\mathbf{N}]\sigma_{\mathrm{n}}\mathrm{d}\Gamma + \int_{\Omega_e} [\mathbf{N}][\mathbf{F}]\mathrm{d}\Omega_e$$
$$\mathbf{K}^j_{\mathrm{TT}} = \int_{\Omega_e} rh[\mathbf{B}_{\mathrm{T}}]'[\mathbf{k}][\mathbf{B}_{\mathrm{T}}]\mathrm{d}\Omega_e \qquad \mathbf{F} = \begin{Bmatrix} F_r \\ 0 \end{Bmatrix}$$

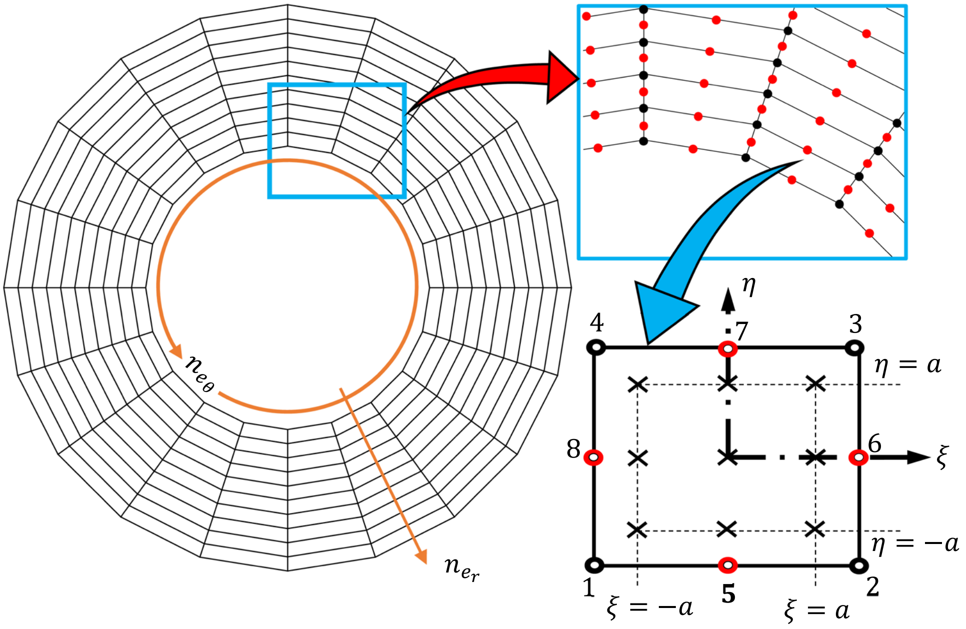

Fig. 14 A two-dimensional mesh for a circular disc using the isoparametric eight-node element with nine gauss integration points. n_{e_r} and n_{e_θ} are the number of finite elements along the radial and tangential directions, respectively. ξ and η are the natural coordinates within the element with $a = \sqrt{3/5}$. Numbers from one to eight refer to the node's number in a counterclockwise manner

where **B** is given as [39]:

$$\mathbf{B}_\mathrm{U} = \begin{bmatrix} N_{,r} & 0 \\ Nr^{-1} & N_{,\theta}r^{-1} \\ N_{,\theta}r^{-1} & N_{,r} - Nr^{-1} \end{bmatrix}_{3\times 2n_n},$$

$$\mathbf{B}_\phi = \mathbf{B}_\mathrm{T} = \mathbf{B}_\mathrm{M} = \begin{bmatrix} N_{,r} \\ N_{,\theta}r^{-1} \end{bmatrix}_{2\times n_n} \qquad \text{(B–3)}$$

In addition, Ω_e represents the element's domain such that $\mathrm{d}\Omega_\mathrm{e} = \mathrm{d}r\mathrm{d}\theta$ and Γ is part of the boundary with specified tractions $\boldsymbol{\sigma}_\mathrm{n}$. It is essential to mention that for the plane strain conditions, $\widetilde{\beta}$ is replaced by β.

See Fig. 14

References

1. Kumar, P.; Harsha, S.P.: Static and vibration response analysis of sigmoid function-based functionally graded piezoelectric non-uniform porous plate. J. Intell. Mater. Syst. Struct. **33**(17), 2197–2227 (2022). https://doi.org/10.1177/1045389X221077433
2. Jabbari, M.; Meshkini, M.; Eslami, M.R.: Nonaxisymmetric mechanical and thermal stresses in FGPPM hollow cylinder. J. Pressure Vessel Technol (2012). https://doi.org/10.1115/1.4007034
3. Jabbari, M.; Sohrabpour, S.; Eslami, M.R.: General solution for mechanical and thermal stresses in a functionally graded hollow cylinder due to nonaxisymmetric steady-state loads. J. Appl. Mech. **70**(1), 111–118 (2003). https://doi.org/10.1115/1.1509484
4. Jabbari, M.; Bahtui, A.; Eslami, M.R.: Axisymmetric mechanical and thermal stresses in thick short length FGM cylinders. Int. J. Press. Vessels Pip. **86**(5), 296–306 (2009). https://doi.org/10.1016/j.ijpvp.2008.12.002
5. Zenkour, A.M.; Abbas, I.A.: Magneto-thermoelastic response of an infinite functionally graded cylinder using the finite element method. J. Vib. Control **20**(12), 1907–1919 (2014). https://doi.org/10.1177/1077546313480541
6. Sarkar, P.R.; Rahman, A.S.: Effect of magnetic field on the thermoelastic response of a rotating FGM circular disk with non-uniform thickness. J. Strain Anal. Eng. Design **57**(2), 116–131 (2022). https://doi.org/10.1177/03093247211005215
7. Eldeeb, A.M.; Shabana, Y.M.; Elsawaf, A.: Thermo-elastoplastic behavior of a rotating sandwich disc made of temperature-dependent functionally graded materials. J. Sandwich Struct. Mater. **23**(5), 1761–1783 (2021). https://doi.org/10.1177/1099636220904970
8. Eldeeb, A.M.; Shabana, Y.M.; Elsawaf, A.: Influences of angular deceleration on the thermoelastoplastic behaviors of nonuniform thickness multilayer FGM discs. Compos. Struct. **258**, 113092 (2020). https://doi.org/10.1016/j.compstruct.2020.113092
9. Eldeeb, A.M.; Shabana, Y.M.; Elsawaf, A.: Investigation of the thermoelastoplastic behaviors of multilayer FGM cylinders. Compos. Struct. **276**, 114523 (2021). https://doi.org/10.1016/j.compstruct.2021.114523
10. Khoshgoftar, M.J.; Ghorbanpour Arani, A.; Arefi, M.: Thermoelastic analysis of a thick walled cylinder made of functionally graded piezoelectric material. Smart Mater. Struct. **18**(11), 115007 (2009). https://doi.org/10.1088/0964-1726/18/11/115007
11. Ghorbanpour, A., et al.: Electrothermomechanical behavior of a radially polarized rotating functionally graded piezoelectric cylinder. J. Mech. Mater. Struct. **6**(6), 869–882 (2011). https://doi.org/10.2140/jomms.2011.6.869
12. Zenkour, A.M.: Piezoelectric behavior of an inhomogeneous hollow cylinder with thermal gradient. Int. J. Thermophys. **33**(7), 1288–1301 (2012). https://doi.org/10.1007/s10765-012-1248-3
13. Wang, H.M.: Thermally induced piezothermoelastic fields of a smart sandwich cylindrical structure with a functionally graded interlayer. J. Therm. Stresses **37**(5), 585–603 (2014). https://doi.org/10.1080/10510974.2014.884894

14. Wu, C.-P.; Lim, X.-F.: Coupled electro-mechanical effects and the dynamic responses of functionally graded piezoelectric film-substrate circular hollow cylinders. Thin-Walled Struct. **102**, 1–17 (2016). https://doi.org/10.1016/j.tws.2016.01.008
15. Jafari Fesharaki, J., et al.: Two-dimensional solution for electro-mechanical behavior of functionally graded piezoelectric hollow cylinder. Appl. Math. Model. **36**(11), 5521–5533 (2012). https://doi.org/10.1016/j.apm.2012.01.019
16. Atrian, A.; Jafari Fesharaki, J.; Nourbakhsh, S.H.: Thermo-electromechanical behavior of functionally graded piezoelectric hollow cylinder under non-axisymmetric loads. Appl. Math. Mech. **36**(7), 939–954 (2015). https://doi.org/10.1007/s10483-015-1959-9
17. Akbarzadeh, A.H.; Chen, Z.T.: Hygrothermal stresses in one-dimensional functionally graded piezoelectric media in constant magnetic field. Compos. Struct. **97**, 317–331 (2013). https://doi.org/10.1016/j.compstruct.2012.09.058
18. Zenkour, A.M.: Hygrothermoelastic responses of inhomogeneous piezoelectric and exponentially graded cylinders. Int. J. Press. Vessels Pip. **119**, 8–18 (2014). https://doi.org/10.1016/j.ijpvp.2014.02.001
19. Eldeeb, A.M.; Shabana, Y.M.; Elsawaf, A.: Particle swarm optimization for the thermoelastic behaviors of functionally graded rotating nonuniform thickness sandwich discs. Arab. J. Sci. Eng. **48**, 4067–4079 (2023). https://doi.org/10.1007/s13369-022-07351-x
20. Eldeeb, A.M., et al.: A nontraditional method for reducing thermoelastic stresses of variable thickness rotating discs. Sci. Rep. **13**(1), 41598 (2023). https://doi.org/10.1038/s41598-023-39878-w
21. Zhou, S.; Li, Q.: Microstructural design of connective base cells for functionally graded materials. Mater. Lett. **62**(24), 4022–4024 (2008). https://doi.org/10.1016/j.matlet.2008.05.058
22. Nemat-Alla, M.: Reduction of thermal stresses by developing two-dimensional functionally graded materials. Int. J. Solids Struct. **40**(26), 7339–7356 (2003). https://doi.org/10.1016/j.ijsolstr.2003.08.017
23. Ghatage, P.S.; Kar, V.R.; Sudhagar, P.E.: On the numerical modelling and analysis of multi-directional functionally graded composite structures: a review. Compos. Struct. **236**, 111837 (2020). https://doi.org/10.1016/j.compstruct.2019.111837
24. Nemat-Alla, M.; Ahmed, K.I.E.; Hassab-Allah, I.: Elastic–plastic analysis of two-dimensional functionally graded materials under thermal loading. Int. J. Solids Struct. **46**(14), 2774–2786 (2009). https://doi.org/10.1016/j.ijsolstr.2009.03.008
25. Hong, N.T.: Nonlinear static bending and free vibration analysis of bidirectional functionally graded material plates. Int. J. Aerospace Eng. **2020**, 8831366 (2020). https://doi.org/10.1155/2020/8831366
26. Najibi, A.; Shojaeefard, M.H.: Elastic mechanical stress analysis in a 2D-FGM thick finite length hollow cylinder with newly developed material model. Acta Mech. Solida Sin. **29**(2), 178–191 (2016). https://doi.org/10.1016/S0894-9166(16)30106-9
27. Najibi, A.: Mechanical stress reduction in a pressurized 2D-FGM thick hollow cylinder with finite length. Int. J. Press. Vessels Pip. **153**, 32–44 (2017). https://doi.org/10.1016/j.ijpvp.2017.05.007
28. Najibi, A.; Talebitooti, R.: Nonlinear transient thermo-elastic analysis of a 2D-FGM thick hollow finite length cylinder. Compos. B Eng. **111**, 211–227 (2017). https://doi.org/10.1016/j.compositesb.2016.11.055
29. Moussavinezhad, S.M.; Shahabian, F.; Hosseini, S.M.: Two-dimensional stress-wave propagation in finite-length fg cylinders with two-directional nonlinear grading patterns using the mlpg method. J. Eng. Mech. **140**(3), 575–592 (2014). https://doi.org/10.1061/(ASCE)EM.1943-7889.0000678
30. Salehi, A.; Ahmadi, I.: Transient thermal and mechanical stress analysis of 2D-functionally graded finite cylinder: a truly meshless formulation. Iranian J Sci. Technol. Trans. Mech. Eng (2021). https://doi.org/10.1007/s40997-021-00432-6
31. Miao, X.-Y., et al.: Free vibration analysis of three-layer thin cylindrical shell with variable thickness two-dimensional FGM middle layer under arbitrary boundary conditions. J. Sandwich Struct. Mater. **24**(2), 973–1003 (2021). https://doi.org/10.1177/10996362211020429
32. Meshkini, M., et al.: Asymmetric mechanical and thermal stresses in 2D-FGPPMs hollow cylinder. J. Therm. Stress. **40**(4), 448–469 (2017). https://doi.org/10.1080/01495739.2016.1249987
33. Najibi, A. and Jing, G.: Two dimensional stress wave propagation analysis of infinite 2D-FGM hollow cylinder. Waves in Random and Complex Media, 2021: p. 1–18. https://doi.org/10.1080/17455030.2021.1987584.
34. Eldeeb, A.M., et al.: Thermoelastic stresses alleviation for two-dimensional functionally graded cylinders under asymmetric loading. J. Therm. Stresses **46**(1), 59–74 (2023). https://doi.org/10.1080/01495739.2022.2151960
35. Saadatfar, M.; Aghaie-Khafri, M.: Thermoelastic analysis of a rotating functionally graded cylindrical shell with functionally graded sensor and actuator layers on an elastic foundation placed in a constant magnetic field. J. Intell. Mater. Syst. Struct. **27**(4), 512–527 (2016). https://doi.org/10.1177/1045389X15573342
36. Vullo, V. and Vivio, F.: Rotors: Str*ess analysis and design*. 2013: Springer Science & Business Media.
37. Hassani, A., et al.: Semi-exact elastic solutions for thermo-mechanical analysis of functionally graded rotating disks. Compos. Struct. **93**(12), 3239–3251 (2011). https://doi.org/10.1016/j.compstruct.2011.06.001
38. Saadatfar, M. and Zarandi, M.H.: Effect of angular acceleration on the mechanical behavior of an exponentially graded piezoelectric rotating annular plate with variable thickness. Mechanics Based Design of Structures and Machines, 2020: p. 1–17. https://doi.org/10.1080/15397734.2020.1751198.
39. Reddy, J.N. and Gartling, D.K.: *The finite element method in heat transfer and fluid dynamics*. 2010: CRC press.
40. Chawde, D.P.; Bhandakkar, T.K.: Mixed boundary value problems in power-law functionally graded circular annulus. Int. J. Press. Vessels Pip. **192**, 104402 (2021). https://doi.org/10.1016/j.ijpvp.2021.104402
41. Galic, D.; Horgan, C.O.: The stress response of radially polarized rotating piezoelectric cylinders. J. Appl. Mech. **70**(3), 426–435 (2003). https://doi.org/10.1115/1.1572900
42. Bayat, M., et al.: Thermoelastic solution of a functionally graded variable thickness rotating disk with bending based on the first-order shear deformation theory. Thin-Walled Struct **47**(5), 568–582 (2009). https://doi.org/10.1016/j.tws.2008.10.002
43. Akbarzadeh, A.; Pasini, D.: Multiphysics of multilayered and functionally graded cylinders under prescribed hygrothermomagnetoelectromechanical loading. J. Appl. Mech. **81**(4), 041018 (2014). https://doi.org/10.1115/1.4025529
44. Saadatfar, M.; Aghaie-Khafri, M.: Hygrothermal analysis of a rotating smart exponentially graded cylindrical shell with imperfect bonding supported by an elastic foundation. Aerosp. Sci. Technol. **43**, 37–50 (2015). https://doi.org/10.1016/j.ast.2015.02.012
45. Saadatfar, M.; Aghaie-Khafri, M.: On the behavior of a rotating functionally graded hybrid cylindrical shell with imperfect bonding subjected to hygrothermal condition. J. Therm. Stresses **38**(8), 854–881 (2015). https://doi.org/10.1080/01495739.2015.1038487